Long-term Lidar Observations of the Gravity Wave Activity near the Mesopause at Arecibo

Xianchang Yue[1,2], Jonathan S. Friedman[4], Qihou Zhou[5], Xiongbin Wu[1,2], Jens Lautenbach[3]

[1]School of Electronic Information, Wuhan University, Wuhan, 430072, China
5   [2]Collaborative Innovation Center of Geospatial Technology, 129 Luoyu Road, Wuhan, 430072, China
[3]Arecibo Observatory – University of Central Florida, Arecibo, Puerto Rico.
[4]Puerto Rico Photonics Institute, School of Science and Technology, Universidad Metropolitana, Cupey, Puerto Rico.
[5]Electrical and Computer Engineering Department, Miami University, Oxford, Ohio, USA

Correspondence to: Xianchang Yue (yuexc@whu.edu.cn)

10   **Abstract.** 11-years long K Doppler lidar observations of temperature profiles in the mesosphere and lower thermosphere (MLT) between 85 and 100 km, conducted at the Arecibo Observatory, Puerto Rico (18.35°N, 66.75°W), are used to estimate seasonal variations of the mean temperature, the squared Brunt-Väisälä frequency, N^2, and the gravity wave potential energy in a composite year. The following unique features are obtained: 1.) The mean temperature structure shows similar characteristics as a prior report based on a smaller dataset: 2.) The profiles of N^2 usually reach the maxima at or just
15   below the temperature inversion layer when that layer is present. The first complete range-resolved climatology of potential energy of temperature fluctuations in the tropical MLT exhibits an altitude dependent combination of annual oscillation (AO) and semiannual oscillation (SAO). Between 88 to 96 km altitude, the amplitudes of AO and SAO are comparable, and their phases are almost the same and quite close to day of year (DOY) 100. Below 88 km, the SAO amplitude is significantly larger than AO and the AO phase shifts to DOY 200 and after. At 97 to 98 km altitude, the amplitudes of AO and SAO reach
20   their minima, and both phases shift significantly. Above that, the AO amplitude becomes greater. The annual mean potential energy profile reaches the minimum at 91 to 92 km altitude. The altitude-dependent SAO of the potential energy is found to be highly correlated with the satellite observed mean zonal winds reported in the literature.

1 Introduction

Gravity waves (GWs) are believed to be the primary force driving the large-scale circulation and coupling of different
25   atmospheric layers due to their momentum and energy deposition when breaking or dissipating (Fritts and Alexander, 2003; Lindzen, 1981; Smith, 2012). Gravity waves usually originate from copious tropospheric sources and propagate upward. Their amplitudes grow rapidly with altitude under the condition of atmospheric density decreasing and begin to break or dissipate in the MLT where gravity wave influences have been shown to be strong by various observations (e.g., Baumgarten et al. 2018; 2017; 2015; Cai et al., 2014; Gardner and Liu, 2010; Li et al., 2010; Lu et al., 2009; Yuan et al., 2016). Gravity
30   waves are therefore an essential component in current General Circulation Models (GCMs) [e.g., Liu and Meriwether, 2004;

Picone et al., 2002]. Associated modeling studies have shown that including the effects of GWs is a key to simulate realistic quasi-biennial and semiannual oscillations and other phenomena in the stratosphere and mesosphere [e.g., Dunkerton, 1997; Huang et al. 2010; Xu et al., 2006].

The upward propagations of GWs are often influenced by the background wind fields (e.g., Yigit and Medvedev, 2017). The altitude ranges, where GWs interact with the background wind dissipating and deposing energy and momentum is of high interest to researchers. This happens mainly in the middle atmosphere near or between stratopause and mesopause. Above 35 km altitude, the semiannual oscillation (SAO) shows a predominance in the annual variability of the zonal winds (e.g., Garcia et al., 1997; Hirota, 1980). The SAO phase of zonal winds shifts approximately 180° with the altitude increasing from stratosphere to mesosphere. The GWs penetrated to the mesosphere are filtered by the stratospheric SAO leading to specific seasonal variations of GW activity in the mesosphere.

The mean zonal winds in mesosphere and lower thermosphere (MLT) have been measured by both ground-based radar (e.g.,, Garcia et al., 1997; Lieberman et al., 1993) and satellites such as the High-Resolution Doppler Imager (HRDI), Wind Imaging Interferometer (WINDII) and the Microwave Limb Sounder (MLS) on board the Upper Atmosphere Research Satellite (UARS) or the Doppler Interferometer (TIDI) on board the Thermosphere Ionosphere Mesosphere Energetics and Dynamics (TIMED) satellite e.g.,, Smith, 2012. They show different features of the zonal winds above and below about 80 km. Garcia et al. (1997) and Smith (2012) showed that, in tropical MLT, the easterly winds in equinoxes seasons decreased with altitude from 80 km above and turned to increase above ~ 95 km. Therefore, the zonal winds are low or zero around 91 km altitude. The zero-wind lines will enhance damping or dissipating of zonal propagating gravity wave with low to moderate phase speed.

Temperature is a crucial parameter indicating the state of the atmosphere. To measure the temperature in the MLT region, satellite and lidar techniques are developed in recent decades. Satellite measurements have the advantage of resolving large spatial scale wave structures, but the short-term variability in dynamical features gets lost. While for the lidar measurements, they provide a vertical profile of temperature with a suitable temporal and vertical resolution at a particular location. Lidar data can well resolve gravity waves with short and medium periods and their temporal development. The perturbation or standard deviation from zonal mean temperature is often used as a wave activity indicator in the atmosphere. For instance, Offermann et al. (2006) use the temperature measured from CRISTA (CRyogenic Infrared Spectrometers and Telescopes for the Atmosphere) and from SABER (Sounding of the Atmosphere using Broadband Emission Radiometry) to investigate the global wave activity from upper stratosphere to lower thermosphere. They showed quite different wave behaviors below and above their defined 'wave-turbopause' close to but lower than the mesopause. Below the turbopause, the propagation of the wave is significantly dissipated, while above that, the propagation of the wave is almost free.

The damping of GW activity has also been presented by lidar temperature measurements at mid-latitude sites (Mzé et al., 2014; Rauthe et al., 2008). Both Mzé et al. (2014) and Rauthe et al. (2008) showed that the GW activities presented an annual variation with maximum in winter and minimum in summer, they damped significantly at the upper mesosphere altitudes above ~ 70 km in all seasons, while the damping below ~ 70 km is not so eminent. Mzé et al. (2014) almost

observed the conservation of GW potential energy in summer in the low mesosphere. Meanwhile, Rauthe et al. (2008) also reported the weakest damping occurring in the summer seasons. These results suggest more attention should be paid to the observation of the upper mesosphere and mesopause region to improve the GW parameterization in the atmospheric models.

Seasonal variations of GW activities based on lidar temperature measurements have been investigated at few low latitude sites (Chane-Ming et al., 2000; Li et al., 2010; Sivakumar et al., 2006). These researches used Rayleigh lidar data and focused mainly on the upper stratosphere and lower mesosphere in an altitude region from 30 to 80 km. They showed the SAO dominated the seasonal variability of GW activities with maxima in both winter and summer and minima near the equinox. Li et al. (2010) related this to the dominated SAO in the mean zonal wind in the tropical stratosphere and lower mesosphere. Considering the transforming of the mean zonal wind above ~80 km in the tropical region, the seasonal variability of GW activity in the tropical upper mesosphere is expected to be different from either the lower altitudes or the mid- and high-latitude regions.

To our knowledge, the seasonal variability of GW activity retrieved from mesospheric lidar temperature data with high temporal and vertical resolution have never been reported from a tropical location.

Such measurements of atmospheric temperature have been conducted with the K Doppler lidar located at the Arecibo Observatory (18.35°N, 66.75°W), Puerto Rico (Friedman and Chu, 2007; Yue et al., 2013, 2016, 2017). Since December 2003, the Arecibo Observatory K Doppler lidar has operated routinely, producing high-quality temperature data. In this report, we estimate the mean temperature, the squared Brunt-Väisälä frequency, N^2, and the gravity wave potential energy and their annual variability from the temperature dataset. The vertical structures of SAO and AO in these parameters and their relationships are exhibits. We find an altitude-to-altitude close relationship between the annual variability of the potential energy in this report and that of the mean zonal winds in the literature. Their implications to the role of gravity wave in the MLT are discussed.

2 Observations

The Arecibo K Doppler lidar probes the potassium D1 line to deduce the potassium density and neutral air temperature simultaneously by employing the three-frequency technique (e.g., Friedman and Chu, 2007; Friedman et al., 2003). The temperature was obtained at 0.45/0.9 km vertical and 10/30 minutes temporal resolution, respectively (Friedman and Chu, 2007; Yue et al., 2017), and we unify them into profiles with resolutions of 0.9 km and 30 minutes in vertical and temporal dimensions, respectively. This data processing excludes the perturbations relevant to gravity waves with vertical wavelengths and observed periods less than 1.8 km and 1 hour, respectively. Their exclusion may bias the deduced gravity wave associated potential energy estimations towards mid- and low-frequency gravity waves. The root mean square (RMS) temperature errors is about 2 to 3 K at the peak of the K density layer and increase to about 10 K at the edge of the layer around 85 and 100 km (Friedman and Chu, 2007; Yue et al., 2017).

Measurements are made only at night in two periods, one from December 2003 to January 2010, the other from November 2015 to April 2017. Data were available for every calendar month. Across the 11 years of the data collection period, 198 observing nights with a total of 1451 hours of data were available at the time of preparing this report. The number of observation nights/hours varies from 4 nights/27 hours in October, to 32 nights/253 hours in January. On average there are

5 16.5 nights or 121 hours of observation each month. The statistics for the used temperature observations are plotted in Fig. 1 and the numbers of observational nights and durations are summarized for each month in Table 1. When the data are binned into weekly intervals, they cover 45 weeks of a year. On average there are 3.8 nights or 32.2 hours of observation each week. The gaps are at weeks 7,18, 19, 25, 26, 39 and 42. The distribution of the data is quite evenly during the year. This allows us to fit the gravity wave activity annual variability through weekly means of temperature.

10 **3 Calculating Methods**

The gravity wave energy includes kinetic and potential energy. The ratio of kinetic to potential energy can be taken as a constant according to the linear theory of the gravity wave (e.g., Ratnam et al., 2004; Tsuda et al., 2000); therefore, it is possible to estimate gravity wave energy from temperature observations only. The potential energy density E_p is chosen as a measure of GW activity and is defined as (see, e.g., Vincent et al., 1997)

15 $$E_p = \frac{1}{2}\left(\frac{g}{N}\right)^2 \overline{\left(\frac{T'}{\overline{T}}\right)^2},\tag{1}$$

where

$$N^2 = \frac{g}{\overline{T}}\left(\frac{d\overline{T}}{dz} + \frac{g}{C_p}\right),\tag{2}$$

Here g equals to 9.5 ms^{-2}, is the gravitational acceleration in MLT; N is the Brunt-Väisälä frequency calculated according to Eq. (2); $\overline{T}$ is the mean temperature; T' is the temperature perturbation; and C_p is the constant-pressure heat capacity,

20 equals to 1004 JK^{-1}kg^{-1}. In Eq. (1), the calculation of Ep depends on the estimations of N, $\overline{T}$ and T'. The procedure adopted by Gardner and Liu (2007) is closely followed here for the estimation of T'.

The unified 0.9 km and 0.5 h resolution temperature profiles and the extracted temperature perturbation profiles on each observational night in the same week are binned to the same vertical and temporal grids to construct their composite mean night for each week of a year. The weekly composite night data of $\overline{T}$ and T' are first spatially and then temporally smoothed

25 using Hamming windows with full widths at half maximum (FWHM) of 2.7 km and 3 hours, respectively. After that, the weekly composite nights of N^2 and the consequential E_p at 0.9 km and 0.5 h resolutions are estimated through Eq. (2) and (1), respectively. For each parameter, the weekly composite nights are then averaged to derive the weekly mean profiles which are fitted to a model including the annual mean plus 12-month (annual) oscillation and 6-month (semiannual) oscillation.

4 Results and Discussion

In the following the results of the analysis is shown and discussed with respect to the seasonal variation of the mean temperature (4.1), Square of the Brunt-Väisälä frequency (4.2) and seasonal variation of the gravity wave activity (4.3). Therefore, we plot the fitted seasonal variations of $\overline{T}$, N^2, and E_p in Fig. 2a, 3a, and 4a (top left panels), respectively, at 0.9 km vertical and one-week temporal intervals. The amplitudes and phases of the 12-month and 6-month oscillations of the regression model are plotted in Fig. 2c, 3c and 4c (bottom left panels) and 2d, 3d and 4d (bottom right panels), respectively. The annual mean profiles of N^2 and E_p are also plotted in Fig. 3c and 4c. To show the seasonal variation of each parameter more clearly, the data between 87 and 97 km are averaged in altitude and then fitted to the same seasonal model consisting of the annual mean, AO and SAO. The averaged results and the fitted curves are plotted in Fig. 2b, 3b and 4b (top right panels). The statistical parameters for this fit are summarized in Table 2.

4.1 Seasonal Variation of the Mean Temperature

Figure 2a shows that the Arecibo climatology is warmer in late-autumn-early-winter and colder in summer throughout all altitudes. An inversion layer is present most of the time. The altitude of the local maximum of the temperature inversion layer occurs at ~95 km from February to May and descends to ~ 91 km in early June, after which it maintains this altitude until September. The mesopause is above 96 km except in the period from the second half of September to November where it is situated at ~ 96 km. The amplitudes of the AO are obviously larger than that of the SAO as shown in Fig. 2c. The phases (defined as the time of the maximum perturbation) of both AO and SAO are independent of height and located near DOY 110 and 330, respectively. Figure 1b shows that the mean temperature is warmest between October and November and coldest in July. An insignificant secondary peak/trough occurs in April/February. Except for the smaller amplitude of SAO oscillation in this study, the seasonal variation of the mean temperature is consistent with a previous study by Friedman and Chu (2007) (see their Fig. 6 to 7), who used data collected between December 2003 and September 2006.

4.2 Square of the Brunt-Väisälä frequency

The square of the Brunt-Väisälä frequency N^2 is a good indicator to characterize the atmospheric static stability. Gardner and Liu (2007) indicated that the resulting N^2 were usually overestimated in this way due to the eliminations of gravity waves when the weekly mean temperature profiles were derived by employing data averaging. However, they pointed out that the lower- value regions of N^2 represented well the lower stability of the atmosphere, i.e., the greater wave dissipations. Figure 3a shows that the atmosphere is statically stable on average throughout the height range from 85 to 100 km. The region of greater average stability lay just at and below the temperature inversion layers (shown in Fig. 2a) just above the mesopause where the mean temperatures increase with increasing altitude.

The fitted curve of $\overline{N^2}$ (average of N^2 between 87 and 97 km height) as shown in Fig. 3b clearly exhibits seasonal variations. The maximum occurs in July and the minimum between October and November, while a secondary maximum occurs

between January and February and a secondary minimum in May. It is worth to note that $\overline{N^2}$ is larger than 3.5×10-4 s-2 in all months, which indicate that the atmosphere is highly stable in this region over Arecibo.

Figure 3c shows that the annual mean N^2 is larger than 4.0×10-4 s-2 at all altitude. The amplitudes of the 12-month and the 6-month oscillations are comparable throughout most of the altitude range of interest, but their phases fluctuate randomly with altitude as shown in Fig. 3d. The 6-month phase is near DOY 100 (-82) at the bottom and shifts to DOY 80 at the top. Meanwhile, the 12-month phase oscillates in a wide range between DOY 0 (near the bottom) and 290 (-75 in the 96 to 98 km range).

The mean temperature and N^2 profiles exhibit strong seasonal variations. The seasonal variation of the mean temperature and N^2 profiles are used to determine the seasonal variation of gravity wave activity in this region.

4.3 Seasonal Variation of the Gravity Wave Activity

Gravity wave activity is directly manifested by the wave energy. Figure 4a shows that the potential energy always reaches the maximum in equinox seasons below 97 km altitude, and mostly near spring equinox. More interesting, in equinox seasons the potential energy decreases with altitude from the bottom to ~ 91 km and then shifts to increase with altitude in the range from 91 to 95 km. However, the potential energy is quite small and almost constant at 85 to 95 km altitude during solstices. The energies are low near 91 km throughout all the year. Above 91 km and below an obvious semiannual oscillation is visible at all altitudes in Fig. 3a. The oscillations of potential energy become very weak around 97 km.

Figure 4c shows that the annual mean profile of potential energy reaches its minimum around 91 to 92 km altitude. It increases toward both the top and bottom edge. The amplitudes of both the 12-month and the 6-month oscillations are comparable and significant in a height range from about 88 to 95 km. The amplitude of 6-month oscillation is larger below about 88 km but smaller above 95 km. Both amplitudes reach their minima near 97 to 98 km altitude. The phase of 6-month oscillation is almost independent of altitude. It is quite close to DOY 100 except that it is close to DOY 10 in the 97 to 98 altitude range. The 12-month oscillation has almost the same phase as the 6-month oscillation from 88 to 96 km altitude. Its phase shifts to the end of the year near the top edge where it is the dominant seasonal variation.

4.4 Discussion

In retrospect to the scientific literature in SAO studies, the features of gravity wave potential energy characterized above can be easily connected to the seasonal cycle of zonal winds measured by HRDI (see e.g., Fig. 3 in Garcia et al. 1997; Fig. 3 in Smith 2012). In equinox seasons, the decrease and then increase of gravity wave potential energy relates closely to the fact that the prevailing easterly winds decreases with altitude below ~91 km and then shifts to increase with altitudes above and reaches a maximum just below 100 km altitude. The stronger potential energy in spring equinox season compared to autumn equinox season agrees well with larger easterly winds in spring than in autumn. In solstice seasons, the constantly low potential energy below about 92 km is in accordance with the always prevailing westerly winds in this region. In these

seasons, the HRDI westerly winds constantly decrease with altitude from below and turn to westerly winds above ~ 91 km. The increase of potential energy above 91 km in summer and winter is corresponding to the slow development of easterly winds. Near the 91 to 92 km altitude range, where the annual mean profile of potential energy reaches the minimum, the HRDI winds reach zero or near zero in all seasons. At 97 to 98 km altitude range, where the magnitudes of AO and SAO in

5   potential energy reach the minima, the HRDI winds also oscillate slightly throughout the year. These close relationships between the gravity wave potential energy estimated here and the HRDI zonal winds reported in the literature suggest the effect of filter by the mean winds. The propagations of gravity waves are favored at easterly winds and they are enhanced to damp or dissipate when the easterly winds become weaker; the gravity wave is filtered out when the westerly winds are prevailing. It is also suggested that the temperature perturbations can be excited locally, the strength of the perturbations is in

10   good scale with the magnitude of zonal winds.

For freely propagating GWs, the potential energy per unit mass (J.kg-1) should increase exponentially with altitude for the conservation of energy. Fig 4a shows that the potential energy decreases firstly and then turn to increases gradually with altitude below ~ 95 km in all seasons. Above ~ 95 km, the GW potential energy enhanced significantly with altitude. This feature is clearly shown by the annual mean potential energy profile in Fig. 4c. The solid curve varies slightly below ~ 95 km

15   but turns to increase exponentially with altitude above. This behavior of mean potential energy is much similar to that retrieved from satellite temperature data (Offermann et al., 2006, see their Figures 10 and 11). The altitude of ~ 95 km is in the vicinity of their 'wave-turbopause' altitude range, and close to the mesopause over this site [Friedman and Chu, 2007; Yue et al., 2017]. This result indicates that the GW damps significantly dissipating or deposing energy below about the mesopause (or the wave-turbopause defined by Offermann et al. 2016), but it propagates upward almost freely after

20   penetrating to the thermosphere.

SAO is the main feature for the seasonal variability of the GW activity in the tropical upper mesosphere. The maxima occur in both spring and autumn and the minima near solstice. However, the SAO in the GW activity in the tropical lower mesosphere reaches the maxima in both summer and winter and the minima near equinox [e.g., Li et al., 2010]. The transforming of GW activity phase from solstice to equinox with altitude from lower to upper mesosphere coincides well

25   with the seasonal transforming of mean zonal wind phase in this region. This suggests that the filter of mean wind fields damps the GWs on one hand, and the deposited energy and momentum by the dissipated GWs impacts on the background mean wind fields on the other hand.

5 Summary and Conclusion

A seasonal analysis of gravity wave activity in the tropical mesopause region is present using 11 years long nocturnal

30   temperature measurements by the K Doppler lidar over the Arecibo Observatory. The mean temperature $\overline{T}$, the square of the Brunt-Väisälä frequency N^2 and the potential energy of perturbation associated with gravity waves E_p are estimated with high accuracy and resolution from the temperature data. All these parameters exhibit obvious AO and SAO harmonics, the

phases of AO and SAO are random with altitude for $\overline{T}$ and N^2, but are independent of altitude and close to DOY 100 at most altitudes for E_p. The annual mean profile of potential energy reaches the minimum at 91 to 92 km altitude range. The amplitudes of AO and SAO for potential energy reach the minima at 97 to 98 km altitude.

The seasonal variations and vertical structures of E_p relate closely to the HRDI zonal winds reported in the literature. These relationships imply that the gravity wave activities are determined by the filtered-out and dissipating effects of background winds for one aspect and by the local excitation due to the background winds for the other aspect. The gravity-wave-filter-out effects in solstice seasons and the stronger damp or dissipation of the gravity wave in spring equinox than in autumn equinox means that there is almost no energy or momentum of gravity wave deposited in summer and winter, but there are more energy or momentum deposited in spring and autumn with the largest deposition in autumn. This sequitur also helps to understand the seasonal variations of the mean profiles of atmospheric temperature in MLT over Arecibo.

Competing interests. The authors declare that they have no conflict of interest.

Acknowledgments. The study is supported by NSFC grant 41474128, 61771352 and NSF grants AGS-1243133. The Arecibo Observatory is operated by The University of Central Florida under a cooperative agreement with the National Science Foundation (AST-1744119) and in alliance with Yang Enterprises and Ana G. Méndez -Universidad Metropolitana. The authors thank Dr. John Anthony Smith, Dr. Frank Djuth, Dr. Dave Hysell, Dr. Min-Chang Lee and Eframir Franco Diaz for their help with the observations.

References

Baumgarten, G., Fiedler, J., Hildebrand, J., and Lübken, F.-J.: Inertia gravity wave in the stratosphere and mesosphere observed by Doppler wind and temperature lidar, Geophys. Res. Lett., 42, 10929–10936, https://doi.org/10.1002/2015GL066991, 2015.

Baumgarten, K., Gerding, M., and Lübken, F.-J.: Seasonal variation of gravity wave parameters using different filter methods with daylight lidar measurements at midlatitudes, J. Geophys. Res.-Atmos., 122, 2683–2695, https://doi.org/10.1002/2016JD025916, 2017.

Baumgarten, K., Gerding, M., Baumgarten, G., and Lübken, F.-J.: Temporal variability of tidal and gravity waves during a record long 10-day continuous lidar sounding, Atmos. Chem. Phys., 18, 371-384, https://doi.org/10.5194/acp-18-371-2018, 2018.

Cai, X., Yuan, T., Zhao, Y., Pautet, P. D., Taylor, M. J., and Pendleton, Jr W. R.: A coordinated investigation of the gravity wave breaking and the associated dynamical instability by a Na lidar and an Advanced Mesosphere Temperature Mapper over Logan, UT (41.7°N, 111.8°W), J. Geophys. Res.-Space, 119, 6852–6864, https://doi.org/10.1002/2014JA020131, 2014.

Chane-Ming, F., Molinaro, F., Leveau, J., Keckhut, P., and Hauchecorne A.: Analysis of gravity waves in the tropical middle atmosphere over La Reunion Island (21°S, 55°E) with lidar using wavelet techniques, Ann. Geophys., 18, 485 –498, https://doi.org/10.1007/s00585-000-0485-0, 2000.

Dunkerton, T. J.: Theory of the Mesopause Semiannual Oscillation, J. of Atmos. Sci., 39, 2681–2690, 1982.

5 Fritts, D. C., and Alexander, M. J.: Gravity wave dynamics and effects in the middle atmosphere, Rev. Geophys., 41, 1003, https://doi.org/10.1029/2001RG000106, 2003.

Friedman, J. S., Tepley, C. A., Raizada, S., Zhou, Q. H., Hedin, J., and Delgado, R.: Potassium Doppler-resonance lidar for the study of the mesosphere and lower thermosphere at the Arecibo Observatory, J. Atmos. Solar-Terr. Phys., 65, 1411-1424, 2003.

10 Friedman, J. S., and Chu, X.: Nocturnal temperature structure in the mesopause region over the Arecibo Observatory (18.35°N, 66.75°W): Seasonal variations, J. Geophys. Res.-Atmos., 112, D14107, https://doi.org/10.1029/2006JD008220, 2007.

Garcia, R. R., Dunkerton, T. J., Lieberman, R. S., and Vincent, R. A.: Climatology of the semiannual oscillation of the tropical middle atmosphere, J. Geophys. Res.-Atmos., 102, 26019-26032, https://doi.org/10.1029/97JD00207, 1997.

15 Gardner, C. S., and Liu, A, Z.: Seasonal variations of the vertical fluxes of heat and horizontal momentum in the mesopause region at Starfire Optical Range, New Mexico, J. Geophys. Res.-Atmos., 112, D09113, https://doi.org/10.1029/2005JD006179, 2007.

Gardner, C. S., and Liu, A. Z.: Wave-induced transport of atmospheric constituents and its effect on the mesospheric Na layer, J. Geophys. Res.-Atmos., 115, D20302, https://doi.org/10.1029/2010JD014140, 2010.

20 Hirota, I.: Observational evidence of the semiannual oscillation in the tropical middle atmosphere – A review, Pure Appl. Geophys., 118, 217–238, https://doi.org/10.1007/BF01586452, 1980.

Li, T., Leblanc, T., McDermid, I. S., Wu, D. L., Dou, X., and Wang, S.: Seasonal and interannual variability of gravity wave activity revealed by long-term lidar observations over Mauna Loa Observatory, Hawaii, J. Geophys. Res.-Atmos., 115, D13103, https://doi.org/10.1029/2009JD013586, 2010.

25 Lieberman, R. S., Burrage, M. D., Gell, D. A., Hays, P. B., Marshall, A. R., Ortland, D. A., … Franke, S. J.: Zonal mean winds in the equatorial mesosphere and lower thermosphere observed by the High Resolution Doppler Imager, Geophys. Res. Lett., 20, 2849-2852, https://doi.org/10.1029/93GL03120, 1993.

Lindzen, R. S.: Turbulence and stress owing to gravity wave and tidal breakdown, J. Geophys. Res., 86, 9707-9714, https://doi.org/10.1029/JC086iC10p09707, 1981.

30 Lu, X., Liu, A. Z., Swenson, G. R., Li, T., Leblanc, T., and McDermid, I. S.: Gravity wave propagation and dissipation from the stratosphere to the lower thermosphere, J. Geophys. Res.-Atmos., 114, D11101, https://doi.org/10.1029/2008JD010112, 2009.

Mzé, N., Hauchecorne, A., Keckhut, P., and Thétis, M.: Vertical distribution of gravity wave potential energy from long-term Rayleigh lidar data at a northern middle-latitude site, J. Geophys. Res.-Atmos., 119, 12,069–12,083, https://doi.org/10.1002/2014JD022035, 2014.

Offermann, D., Jarisch, M., Oberheide, J., Gusev, O., Wohltmann, I., Russell III, J. M., and Mlynczak, M. G.: Global wave activity from upper stratosphere to lower thermosphere: A new turbopause concept, J. Atmos. Solar-Terr. Phys., 68, 1709–1729, https://doi.org/10.1016/j.jastp.2006.01.013, 2006.

Ratnam, M.V., Tetzlaff, G., and Jacobi, C.: Global and Seasonal Variations of Stratospheric Gravity Wave Activity Deduced from the CHAMP/GPS Satellite, J. Atmos. Sci., 61, 1610-1620, 2004.

Rauthe, M., Gerding, M., and Lübken, F.-J.: Seasonal changes in gravity wave activity measured by lidars at mid-latitudes, Atmos. Chem. Phys., 8, 6775-6787, https://doi.org/10.5194/acp-8-6775-2008, 2008.

Sivakumar, V., Rao, P. B., and Bencherif, H.: Lidar observations of middle atmospheric gravity wave activity over a low-latitude site (Gadanki, 13.5°N, 79.2°E), Ann. Geophys., 24, 823–834, https://doi.org/10.5194/angeo-24-823-2006, 2006.

Smith, A.: Global Dynamics of the MLT, Surv. Geophys., 33, 1177-1230, 2012.

Tsuda, T., Nishida, M., Rocken, C., and Ware, R. H. A global morphology of gravity wave activity in the stratosphere revealed by the GPS occultation data (GPS/MET), J. Geophys. Res.-Atmos., 105, 7257-7273, https://doi.org/10.1029/1999JD901005, 2000.

Vincent, R. A., Allen, S. J., and Eckermann, S. D.: Gravity Wave Processes: Their Parameterization in Climate Models, NATO ASI Series, Gravity wave parameters in the lower stratosphere, K. Hamilton, 150, Springer,7–25, 1997.

Yuan, T., Heale, C.J., Snively, J.B., Cai, X., Pautet, P.-D., Fish, C., … Mitchell, N. J.: Evidence of dispersion and refraction of a spectrally broad gravity wave packet in the mesopause region observed by the Na lidar and Mesospheric Temperature Mapper above Logan, Utah, J. Geophys. Res.-Atmos., 121, 579–594, https://doi.org/10.1002/2015JD023685, 2016.

Yue, X., Zhou, Q., Raizada, S., Tepley, C., and Friedman, J.: Relationship between mesospheric Na and Fe layers from simultaneous and common-volume lidar observations at Arecibo, J. Geophys. Res.-Atmos., 118, 905–916, https://doi.org/10.1002/jgrd.50148, 2013.

Yue, X., Zhou, Q., Yi, F., Friedman, J., Raizada, S., and Tepley, C.: Simultaneous and common-volume lidar observations of K/Na layers and temperature at Arecibo Observatory (18°N, 67°W), J. Geophys. Res.-Atmos., 121, 8038-8054, https://doi.org/10.1002/2015JD024494, 2016.

Yue, X., Friedman, J. S., Wu, X., and Zhou, Q. H.: Structure and seasonal variations of the nocturnal mesospheric K layer at Arecibo, J. Geophys. Res.-Atmos., 122, 7260-7275. https://doi.org/10.1002/2017JD026541, 2017.

Table 1. Arecibo K lidar temperature data used in this study (Days/Hours) by month.

month	Total D/H[a]	2004 D/H	2005 D/H	2006 D/H	2007 D/H	2008 D/H	2009 D/H	2010 D/H	2015 D/H	2016 D/H	2017 D/H
Jan.	21/253	4/27		4/44	2/14	6/34		4/35		7/62	5/43
Feb.	7/101		5/33							4/38	3/31
Mar.	20/135	2/9	10/74		4/30	1/4	3/19				
Apr.	21/149	1/5	14/103	3/16		1/8	2/12				1/8
May	6/45	2/12	2/18	2/10							
Jun.	8/62	3/21	2/16				1/1			3/25	
Jul.	18/112	6/41	1/8	1/9		5/26	5/30				
Aug.	16/112	7/46	4/27	2/11	1/6	2/10				2/14	
Sep.	12/107		6/41	4/36		1/8				3/24	
Oct.	4/27	1/5	3/23								
Nov.	11/152	1/2	5/46	4/31			1/9		4/34	3/33	
Dec.	16/196	1/5	4/30	2/19			6/42	3/27[b]	3/36	5/39	
Total	**198/1451**	**28/171**	**56/417**	**22/163**	**7/50**	**16/88**	**18/113**	**7/62[c]**	**7/70**	**27/235**	**9/82**

[a] D/H stands for Days/Hours; [b] Observed in 2003; [c] Including the observations in 2003.

Table 2. Parameters of mean temperature, temperature variance, squared Brunt-Väisälä frequency and potential energy averaged between 87 and 97 km.

	Annual	Amplitude		Phase (days)		RMS
	Mean	12-month	6-month	12-month	6-month	Residual
Mean temperature (K)	188.7	3.6	1.8	-34	-57	5.5
$\overline{N^2}$ **(10^{-4}s^{-2})**	4.37	0.09	0.12	160	22	0.37
Potential Energy (Jkg^{-1})	351.8	55.9	42.1	119	-89	141.6
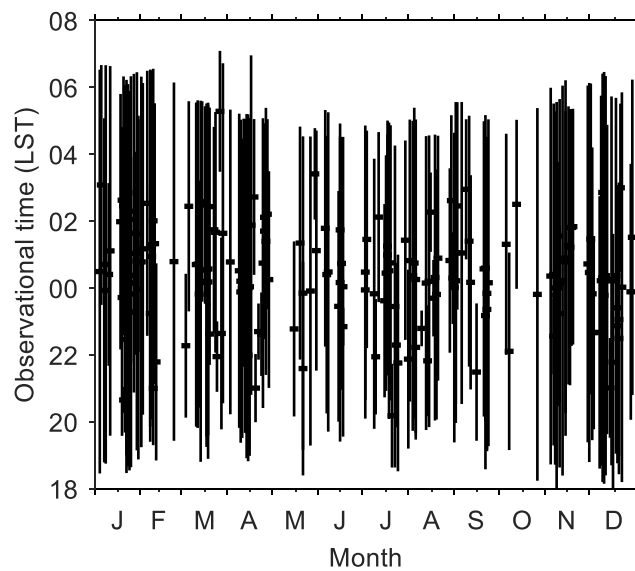
Figure 1: Local time coverage of the used temperature data observed by the K-Doppler lidar at Arecibo from December 2003 to January 2010, and from November 2015 to April 2017.
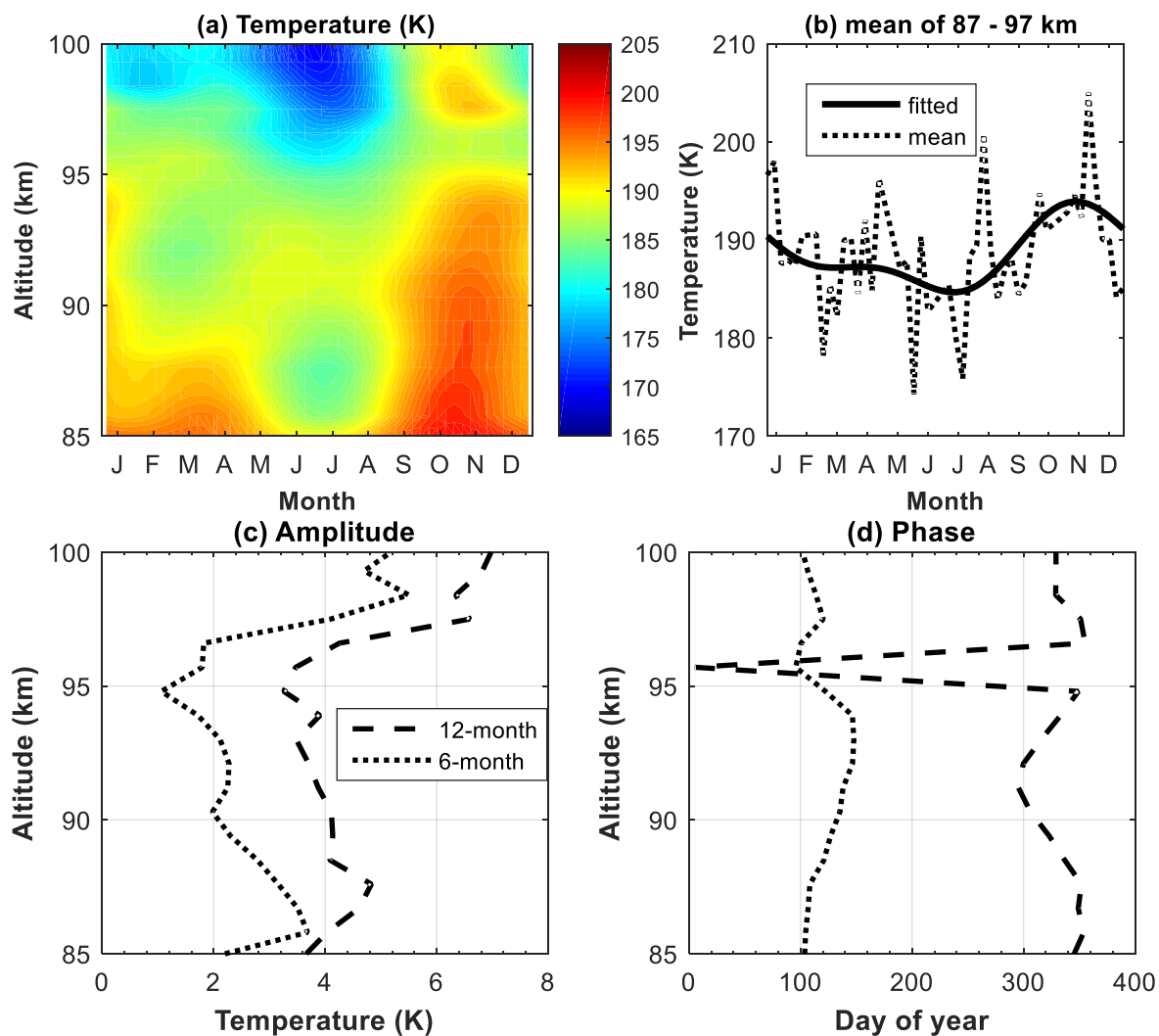
Figure 2: (a) Seasonal variations of night time temperature plotted versus altitude and month, **(b)** seasonal variation of mean temperature between 87 and 97 km, **(c)** 12-month (dashed) and 6-month (dotted) amplitudes and **(d)** 12-month (solid) and 6-month (dotted) phases.
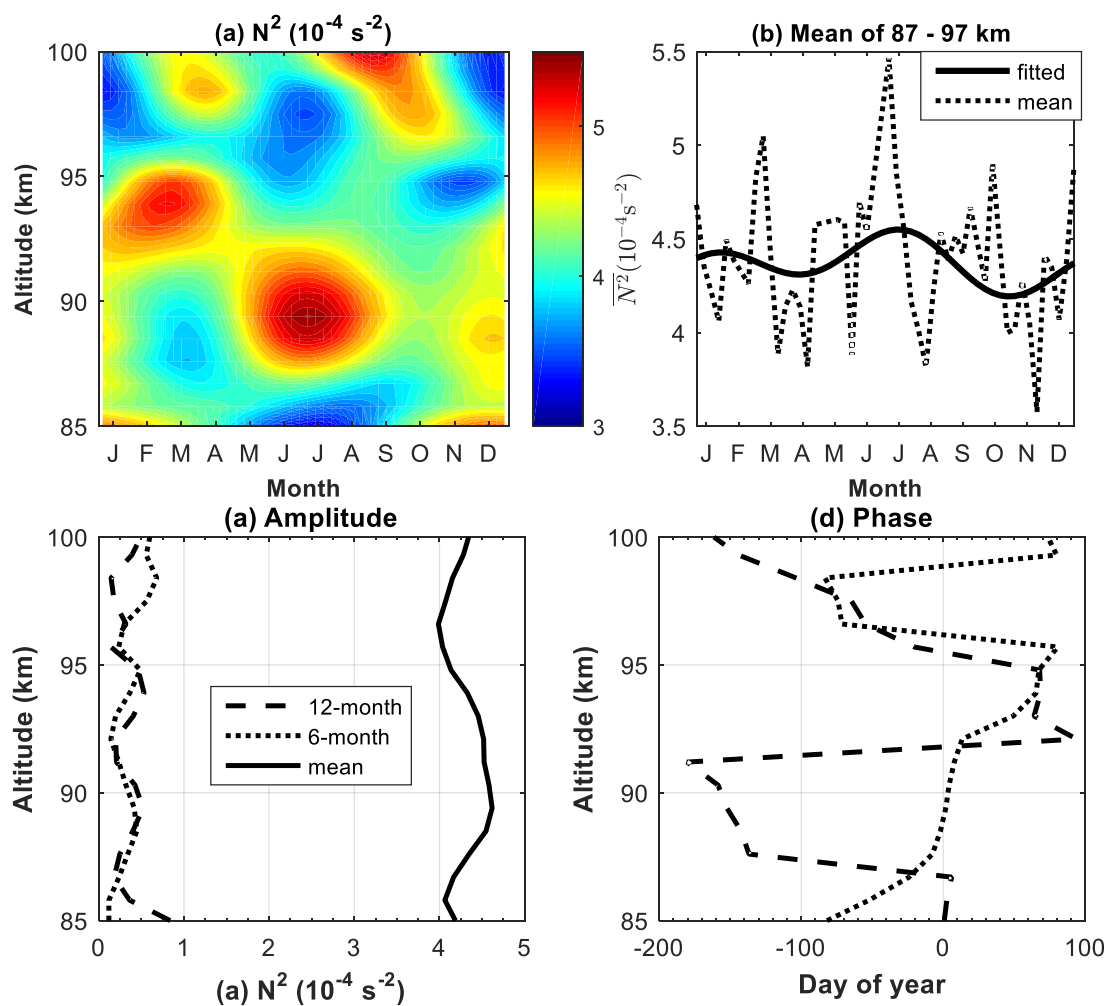
Figure 3: (a) Seasonal variations of squared Brunt-Väisälä frequency N2 plotted versus altitude and month, (b) seasonal variation of mean N2 between 87 and 97 km, (c) annual mean profile (solid) and 12-month (dashed) and 6-month (dotted) amplitudes and (d) 12-month (dashed) and 6-month (dotted) phases.
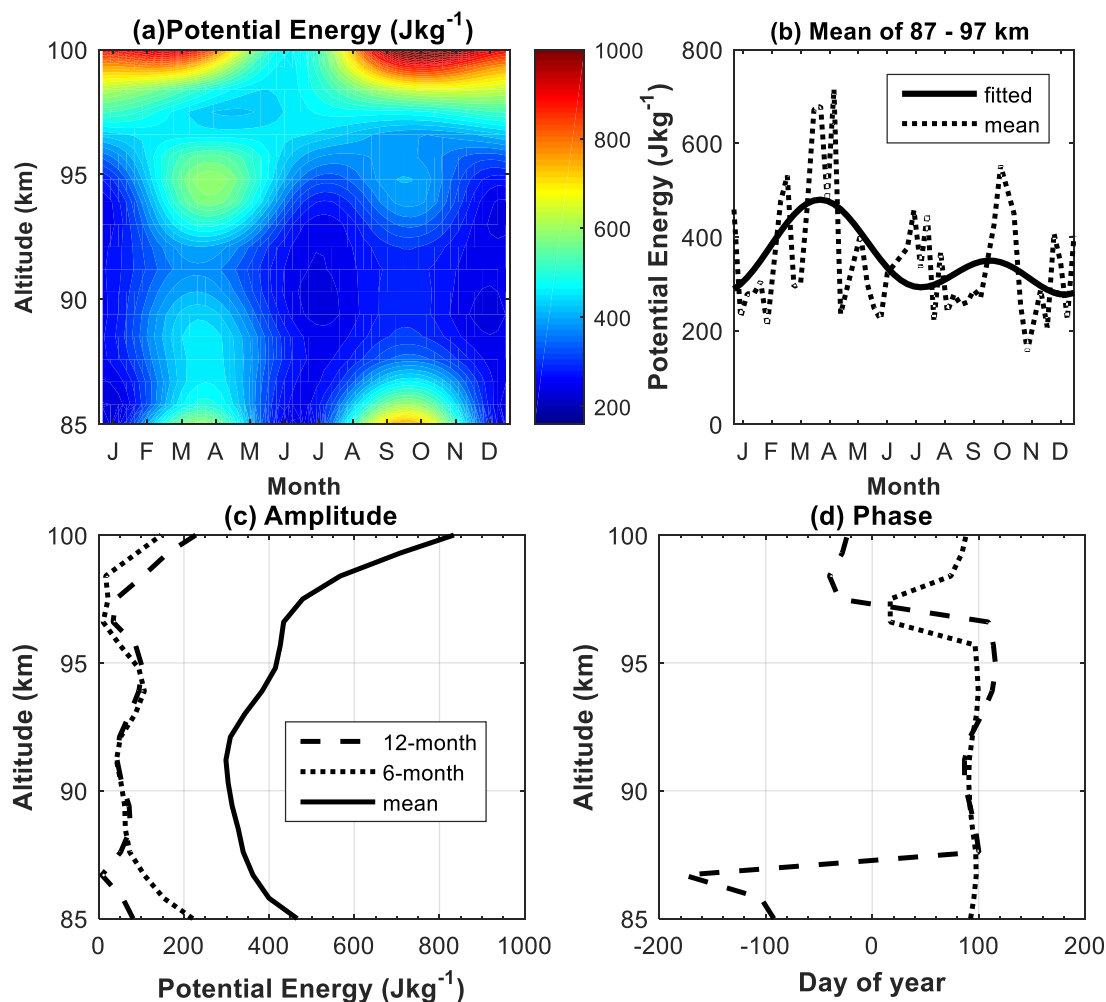
Figure 4: (a) Seasonal variations of squared potential energies plotted versus altitude and month, (b) seasonal variation of mean potential energy between 87 and 97 km, (c) annual mean profile (solid) and 12-month (dashed) and 6-month (dotted) amplitudes and (d) 12-month (dashed) and 6-month (dotted) phases.